Inorg. Chem. **2009**, *48*, 138−148

Structure and Magnetism of $[n\text{-}BuNH_3]_{12}[Cu_4(GeW_9O_{34})_2]\cdot 14H_2O$ Sandwiching a Rhomblike Cu_4^{8+} Tetragon through α-Keggin Linkage

Toshihiro Yamase,*,†,§ Hiroko Abe,† Eri Ishikawa,† Hiroyuki Nojiri,‡ and Yuhgo Ohshima‡

Chemical Resources Laboratory, Tokyo Institute of Technology, R1-21 4259 Nagatsuta, Midori-ku, Yokohama 226-8503 Japan, MO Device, 2-14-10 Kanaiwa-higashi, Kanazawa 920-0335 Japan, and Institute for Material Research, Tohoku University, 2-1-1 Katahira, Aoba-ku, Sendai 980-8577 Japan

Received July 16, 2008

A sandwich-type polyoxometalate, $[Cu_4(GeW_9O_{34})_2]^{12-}$ (**1a**), in which two B-α-$[GeW_9O_{34}]^{12-}$ ligands sandwich a rhomblike Cu_4^{8+} tetragon through α-Keggin linkage, is first isolated as a $[n\text{-}BuNH_3]^+$ salt, $[n\text{-}BuNH_3]_{12}[Cu_4(GeW_9O_{34})_2]\cdot 14H_2O$ (**1**). A Cu_4O_{14} cluster for the rhomblike Cu_4^{8+} tetragon in **1a** with C_{2h} local symmetry consists of two Jahn−Teller (JT) distorted CuO_6 octahedra (at internal sites) with a short diagonal $Cu_{int}\cdots Cu_{int}$ distance of 3.10−3.11 Å and two CuO_5 square pyramids (at external site) with a long diagonal $Cu_{ext}\cdots Cu_{ext}$ distance of 5.34−5.35 Å, the feature of which is different from $[Cu_4(H_2O)_2(GeW_9O_{34})_2]^{12-}$ (**2a**), comprising the four JT-distorted CuO_6 octahedral Cu_4^{8+} tetragons through β-Keggin linkage: the axial Cu_{ext}−O bond distance (2.27−2.29 Å) for **1a** is shorter than the corresponding JT-axial distance (2.36 Å) for **2a**. Measurements of magnetic susceptibility, magnetization, and electron spin resonance spectroscopy for **1** are carried out for better understanding of the molecular magnetism of the Cu_4^{8+} tetragon in comparison with **2a**. The analysis of the magnetic behavior, based on the isotropic Heisenberg spin Hamiltonian comprising three exchange parameters (J, J', and J''), gives $J = -24.1$ cm^{-1} for the $Cu_{ext}\cdots Cu_{int}$ sides, $J' = -99.1$ cm^{-1} for the $Cu_{int}\cdots Cu_{int}$ diagonal, and $J'' = +0.04$ cm^{-1} for the $Cu_{ext}\cdots Cu_{ext}$ diagonal of the Cu_4^{8+} rhombus. The $S = 1$ ground state of **1** displays $g_{\|} = 2.42$, $g_{\perp} = 2.07$, $D = -1.44\times 10^{-2}$ cm^{-1}, and $|A_{Cu\|}| = 46.5\times 10^{-4}$ cm^{-1}. An observation of the asymmetric magnetization between a positive and a negative pulsed field (up to 10^3 T/s) at 0.5 K on the hysteresis loop indicates the quantum tunneling at zero field. The magnetic exchange interactions of four unpaired $d_{x^2-y^2}$-electron spins are discussed in terms of the point-dipole approximation, and the primary contribution to D is implied to come from the magnetic dipole−dipole interaction between two spins at the Cu_{ext} centers.

Introduction

Much attention has been paid to magnetically significant polyoxometalates as model systems for better understanding of the exchange interaction of magnetic clusters, which is very important in research areas of molecular magnetism and bioinorganic chemistry.[1] Their suitability as models is based on the following points: (i) polyoxometalates can coordinate moieties of paramagnetic ions with unusual geometries and highly symmetrical topologies at specific sites of their structures; (ii) such magnetic centers embedded in the structures are isolated from the neighboring molecules with a variety of sizes and high stability due to diamagnetic frameworks of polyoxometalate ligands; (iii) modification of the magnetic centers is possible by modifying the structure, symmetry, and size of polyoxometalate ligands. We have shown the spin-frustrated $(VO)_3^{6+}$ triangle sandwiched by two diamagnetic α-B-$[XW_9O_{33}]^{9-}$ (X = Sb^{III} and Bi^{III}) ligands in local D_{3h} symmetry using $[(VO)_3(SbW_9O_{33})_2]^{12-}$ and $[(VO)_3(BiW_9O_{33})_2]^{12-}$ as a simple model of the magnetization (involving Dzyaloshinsky−Moriya interaction) between pure quantum states $S = 1/2$ and $S = 3/2$.[2] Together with a subsequent effort to provide clear-cut evidence for the Dzyaloshinsky−Moriya interaction inducing half-step magnetization by using single crystals of $[\{Cu(H_2O)\}_3(SbW_9O_{33})_2]^{12-}$,[3] this let us investigate the magnetochemistry

* Author to whom correspondence should be addressed: Fax: + 81-45-924-5260 and +81-76-267-0468. E-mail: tyamase@res.titech.ac.jp and yamase.modevice@nifty.com.
† Tokyo Institute of Technology.
§ MO Device.
‡ Tohoku University.

10.1021/ic8013267 CCC: $40.75
Published on Web 12/04/2008

of a variety of the spin rings embedded in polyoxometalates in order to gain an understanding of the quantum hysteresis of spin rings at the molecular level. We have shown ferromagnetism of the D_{3d}-symmetric Cu_6^{12+} and Mn_6^{12+} hexagons in $[(CuCl)_6(AsW_9O_{33})_2]^{12-}$ and $[(MnCl)_6(SbW_9O_{33})_2]^{12-}$,[4] and we subsequently showed the 1/3 magnetization anomaly of the Mn_6 triangular spin-prism in $[Mn_6(H_2O)_2(AsW_9O_{34})_2(AsW_6O_{26})]^{17-}$, which originates from a delicate balance of exchange interaction.[5] In our continuing work on the synthesis and magnetism of magnetically significant novel polyoxometalates, we have synthesized a novel Cu_4^{8+} tetragon isomer, $(n\text{-}BuNH_3)_{12}[Cu_4(GeW_9O_{34})_2]\cdot 14H_2O$ (**1**), the anion (**1a**) of which consists of a rhomblike Cu_4^{8+} tetragon sandwiched by α-B-$[GeW_9O_{34}]^{10-}$ ligands through α-Keggin linkage. So far, a number of the polyoxometalates consisting of two α-B-$[XW_9O_{34}]^{n-}$ (X = P^V, As^V, Si^{IV}, Ge^{IV}) ligands and a rhomblike four-transition-metal (M) tetragon have been prepared, and all of the anion structures have been characterized as $[M_4(H_2O)_2(XW_9O_{34})_2]^{n-}$ with the β-Keggin linkage.[6] Although magnetochemistry of such a well-isolated spin cluster of $M_4(H_2O)_2$ (M = Cu^{2+}, Co^{2+}, Ni^{2+}) has been also developed,[6c−f,j] surprisingly, there has been neither indication nor magnetochemistry of the complex with the α-Keggin linkage. In our complex, $[Cu_4(GeW_9O_{34})_2]^{12-}$ (**1a**), the rhomblike Cu_4^{8+} tetragon comprises two sets of two axially distorted CuO_5 square pyramids at externally long diagonal sites (Cu_{ext}) and two Jahn−Teller (JT) distorted CuO_6 octahedra at internally short diagonal sites (Cu_{int}), in contrast to the β-Keggin linkage compounds where the $Cu_4(H_2O)_2^{8+}$ tetragon consists of all JT-distorted CuO_6 octahedra at the both long and short diagonal sites. Namely, the two aqua ligands are apically coordinated at the long diagonal Cu_{ext} sites. Since the magnetic characterization of the β-Keggin linkage $Cu_4(H_2O)_2^{8+}$ tetragon compounds has been done for $[Cu_4(H_2O)_2(PW_9O_{34})_2]^{10-}$,[6c] $[Cu_4(H_2O)_2(SiW_9O_{34})_2]^{12-}$,[6g] and $[Cu_4(H_2O)_2(GeW_9O_{34})_2]^{12-}$,[6j] the magnetochemistry of the α-Keggin linkage Cu_4^{8+} tetragon in **1** therefore provides a good opportunity for a better understanding of the magnetic exchange interactions in the Cu_4^{8+} tetragon, in comparison with the β-Keggin linkage Cu_4^{8+} tetragon in $Na_{11}Cs_2[Cu_4(H_2O)_2(GeW_9O_{34})_2]Cl\cdot 31H_2O$ (**2**).[6j] In the present comparative study, the synthesis, the crystal structure, and the magnetic properties of **1** are described, and the magnetic exchange interactions of four $d_{x^2-y^2}$-electron spins in the rhomblike Cu_4^{8+} tetragon are discussed in terms of the point-dipole approximation, which emphasizes a significance of the shortened axial Cu_{ext}−O bond distance.

Experimental Section

Syntheses. All chemicals were used as received unless otherwise stated. $Na_{10}[GeW_9O_{34}]\cdot 18H_2O$[7] and β-Keggin linkage compound $Na_{11}Cs_2[Cu_4(H_2O)_2(GeW_9O_{34})_2]Cl\cdot 31H_2O$ (**2**)[6j] were prepared according to the literature methods.

[*n*-BuNH$_3$]$_{12}$[Cu$_4$(GeW$_9$O$_{34}$)$_2$]·14H$_2$O (1). Solid $Na_{10}[GeW_9O_{34}]\cdot 18H_2O$ (1.41 g, 0.5 mmol) was dissolved in water (16 mL) and heated at 40−50 °C for 10 min. $CuCl_2$ (0.13 g, 1.0 mmol) in water (2 mL) was dropped and n-$BuNH_2\cdot HCl$ (0.55 g, 5.0 mmol) in water (2 mL) was added into the solution. A pale green precipitate was repeatedly removed by filtration, and the filtrate was kept for one week at room temperature. Yellowish green crystals (0.27 g, 0.045 mmol) were produced, which were collected by filtration, washed with cold water, and dried in the air. The yield was ∼18% based on W. Anal. calcd (Found): C, 9.71(9.76); H, 2.92 (2.72); N, 2.83 (2.92); Cu, 4.28 (4.23); Ge, 2.44 (2.40); W, 55.72 (55.53). Selected IR data (KBr), ν(cm^{-1}): 1605(m), 1499(m), 1469(m), 1391(w), 1165(w), 1077(w), 937(s), 882(s), 830(m), 774(s), 720(s), 512(m), 491(m), 456(m), 445(m).

X-Ray Crystallography. The crystal structure of **1** was determined at 300 and 10 K. Crystal data of **1** at 300 K: $C_{48}H_{172}N_{12}O_{82}Cu_4Ge_2W_{18}$, MW = 5938.58, space group $P\bar{1}$ (No.2), a = 12.598(7), b = 16.115(10), c = 16.337(10) Å, α = 108.740(7), β = 94.934(6), γ = 98.701(8)°, Z = 1, V = 3072.6 (2) Å^3, ρ = 3.21 gcm^{-3}, μ = 180.25 cm^{-1}, F(000) = 2712. A crystal (with size = 0.10 × 0.10 × 0.09 mm) of **1** was sealed in a Lindemann glass capillary and mounted on the diffractometer. Intensity data for the single-crystal X-ray crystallography of **1** were measured on a Saturn 70VT CCD Rigaku diffractometer with graphite-monochromatized Mo Kα radiation (= 0.7107 Å) at 300 K, loaded by the confocal mirror (VariMax Mo-VT). Data collection proceeded by using ω-scans with a 0.5° scan and χ = 45° in two runs (with 360 frames respectively) of −70.0° < ω < +110.0° and ϕ = 0° and of −70.0° < ω < +110.0° and ϕ = 90°. The crystal-to-detector distance was 45 mm. The exposure rate was 2 s/deg. The detector swing angle was 19.66°. A total of 24 527 reflections (2.2° < θ < 27.5°) were collected, of which 13 483 unique reflections (R_{int} = 0.060) were

(1) (a) Coronado, E.; Gómez-García, C. J. In *Polyoxometallates: From Platonic Solids to Anti-Retroviral Activity*; Pope, M. T., Müller, A., Eds.; Kluwer Academic Publishers: Norwell, MA, 1994; p 233. (b) Coronado, E.; Gómez-Garcia, C. J. *Chem. Rev.* **1998**, *98*, 273. (c) Clemente-Juan, J. M.; Coronado, E. *Coord. Chem. Rev.* **1999**, *193−195*, 361. (d) Clemente-Juan, J. M.; Clemente-León, M.; Coronado, E.; Forment, A.; Gaita-Ariño, A.; Gómez-García, C. J.; Martínez-Ferrero, E. In *Polyoxometalate Chemistry for Nanocomposite Design*; Yamase, T., Pope, M. T., Eds.; Kluwer Academic/Plenum Publishers: Norewell, MA, 2002; p 157. (e) Clemente-Juan, J. M. M.; Coronado, E.; Forment, A.; Gaita-Ariño, A. In *Polyoxometalate Molecular Science, NATO Science series*; Borrás-Alamenar, J. J., Coronado, E., Müller, A., Pope, M. T., Eds.; Kluwer Academic Publishers: Norwell, MA, 2003; p 273.

(2) (a) Yamase, T.; Ishikawa, E.; Fukaya, K.; Nojiri, H.; Taniguchi, T.; Atake, T. *Inorg. Chem.* **2004**, *43*, 8150. (b) Nojiri, H.; Ishikawa, E.; Yamase, T. *Prog. Theor. Phys. Suppl.* **2005**, *159*, 292.

(3) Choi, K.-Y.; Matsuda, Y. H.; Nojiri, H.; Kortz, U.; Hussain, F.; Stowe, A. C.; Ramsey, C.; Dalal, N. S. *Phys. Rev. Lett.* **2006**, *96*, 107202.

(4) (a) Yamase, T. E.; Fukaya, K.; Nojiri, H.; Ohshima, Y. *Inorg. Chem.* **2006**, *45*, 7698. (b) Ohshima, Y.; Nojiri, H.; Fukaya, K.; Yamase, T. *J. Phys. Conf. Ser.* **2006**, *51*, 195.

(5) (a) Fukaya, K.; Yamase, T. *Bull. Chem. Soc. Jpn.* **2007**, *80*, 178. (b) Oshima, Y.; Nojiri, H.; Fukaya, K.; Yamase, T. *J. Phys. Soc. Jpn.* **2008**, *77*, 044706.

(6) (a) Weakley, T. J. R.; Evans, H. T., Jr.; Showell, J. S.; Tourné, G. F.; Tourné, C. M. *J. Chem. Soc., Chem. Commun.* **1973**, 139. (b) Evans, H. T., Jr.; Tourné, G. F.; Tourné, C. M.; Weakley, T. J. R. *J. Chem. Soc., Dalton Trans.* **1986**, 2699. (c) Gómez-García, C. J.; Coronado, E.; Borrás-Almenar, J. *Inorg. Chem.* **1992**, *31*, 1667. (d) Clemente-Juan, J. M.; Andres, H.; Borrás-Alamenar, J. J.; Coronado, E.; Güdel, H.-U.; Aebersold, M.; Kearly, G.; Büttner, H.; Zollinker, M. *J. Am. Chem. Soc.* **1999**, *121*, 10021. (e) Andres, H.; Clemente-Juan, J. M.; Aebersold, M.; Güdel, H.-U.; Coronado, E.; Büttner, H.; Kearly, G.; Melero, J.; Burriel, R. *J. Am. Chem. Soc.* **1999**, *121*, 10028. (f) Clemente-Juan, J. M.; Coronado, E.; Galán-Mascarós, J. R.; Gómez-García, C. J. *Inorg. Chem.* **1999**, *38*, 55. (g) Kortz, U.; Isber, S.; Dickman, M. H.; Ravot, D. *Inorg. Chem.* **2000**, *39*, 2915. (h) Bi, L.-H.; Huang, R.-D.; Peng, J.; Wang, E.-B.; Wang, Y.-H.; Hu, C.-W. *J. Chem. Soc., Dalton Trans.* **2001**, 121. (i) Kortz, U.; Nellutla, S.; Stowe, A. C.; Dalal, N. S.; van Tol, J.; Bassil, B. S. *Inorg. Chem.* **2004**, *43*, 144. (j) Kortz, U.; Nellutla, S.; Stowe, A. C.; Dalal, N. S.; Rauwald, U.; Danquah, W.; Ravot, D. *Inorg. Chem.* **2004**, *43*, 2317.

(7) Hervé, G.; Tézé, A. *Inorg. Chem.* **1977**, *16*, 2115.

used. The structure was solved by a direct method (SHELXS-97) and refined by using the CrystalStructure software package (SHELXL-97) on the basis of 9309 observed reflections with $I > 2\sigma(I)$ and 549 parameters to $R_1 = 0.074$ ($R = 0.102$ all reflections) and $R_w = 0.219$ (refined against $|F^2|$). The highest residual electron density was 5.46 e Å^{-3} at 0.09 Å from the W8 atom (the deepest hole, −4.94 e Å^{-3} at 0.72 Å, was from W6). Lorentz polarization effects and numerical absorption corrections (by using the program Numabs and Shape, T. Higashi, *Program for Absorption Correction*, Rigaku Corporation, Tokyo, 1999) were applied to the intensity data, and H atoms were not indicated in the calculation. Transmission factors were 0.29−0.53. All of the metal (W, Ge, and Cu) and oxygen atoms (except for three O atoms) for the anion were refined anisotropically, and O4, O32, and O33 atoms and all of the C, O, and N atoms for the cation and crystal water molecules were refined isotropically.

We also measured the crystal of **1** at 10 K with an attachment of the gas flow (Rigaku XR-CS) system from liquid He. A crystal (with size = 0.081 × 0.116 × 0.055 mm) of **1** was coated with Paratone-N paraffin oil and mounted in a loop. Crystal data at 10 K: $C_{48}H_{162}N_{12}O_{77}Cu_4Ge_2W_{18}$, MW = 5848.51, space group $P\bar{1}$ (No.2), $a = 12.064(1)$, $b = 16.191(1)$, $c = 16.317(1)$ Å, $\alpha = 110.526(1)$, $\beta = 92.662(1)$, $\gamma = 91.344(1)°$, $Z = 1$, $V = 2977.0(3)$ Å^3, $\rho = 3.26$ g cm^{-3}, $\mu = 185.9$ cm^{-1}, $F(000) = 2662$. Data collection proceeded by using ω-scan with a 0.5° scan and $\chi = 45°$ in two runs (with 360 frames, respectively) of $-70.0° < \omega < +110.0°$ and $\phi = 0°$ and of $-70.0° < \omega < +110.0°$ and $\phi = 90°$. The crystal-to-detector distance was 45 mm. The exposure rate was 5 s/deg. The detector swing angle was 19.75°. A total of 27 093 reflections ($2.2° < \theta < 29.6°$) were collected, of which 16 797 unique reflections (R_{int}=0.023) were used. The structure was solved by a direct method (SHELXS-97) and refined on the basis of 13 757 observed reflections with $I > 2\sigma(I)$ and 701 parameters to $R_1 = 0.031$ ($R = 0.036$ for all reflections) and $R_w = 0.085$ (refined against $|F^2|$). The highest residual electron density was 4.03 e Å^{-3} at 0.75 Å from the N6 atom (the deepest hole, −2.02 e Å^{-3} at 0.15 Å, was from O5). Lorentz polarization effects were applied, and an empirical absorption corrections (multiscan) using equivalent reflections were performed with the program REQAB (R. Jacobson, private communication, 1998). Transmission factors were 1.00−0.68. All of the metal (W, Ge, and Cu) and O atoms for the anion, eight crystallographically independent from nine crystal-water O atoms and 10 crystallographically independent from 12 $[n\text{-BuNH}_3]^+$ cations (C and N), were refined anisotropically. Other atoms, O39, N6, and C21−C24, were isotropically refined, and O39 was refined with a half-occupancy. Tables S1−S4 (Supporting Information) list the bond distances and bond angles at 300 K (Tables S1 and S2) and 10 K (Tables S3 and S4). Further details on the crystal structure investigations may be obtained from Cambridge Crystallographic Data Center (CCDC), e-mail: deposit@ccdc.cam.ac.uk, depository numbers CCDC-695203 $[n\text{-BuNH}_3]_{12}[Cu_4(GeW_9O_{34})_2]\cdot 14H_2O$ (1−300 K) and CCDC-695204 $[n\text{-BuNH}_3]_{12}[Cu_4(GeW_9O_{34})_2]\cdot 9H_2O$ (1−10 K).

Physical Measurements. IR (as KBr pellet) and UV/vis spectra were recorded on Jasco FT-IR 5000 and Jasco V-570 UV−vis-NIR spectrometers, respectively. The contents of Ge, Cu, and W were determined by inductively coupled plasma atomic emission spectroscopy on a Rigaku Spectro CIROS^{CCD} spectrometer. The magnetic susceptibility in the range 1.8−300 K was measured with a Quantum Design MPMS-XL5 SQUID magnetometer, and the experimental data were corrected for the contribution of the sample holder and for the diamagnetism of the sample estimated from Pascal's constants.[8] X-band electron spin resonance (ESR) measurements were carried out on a JEOL ESR spectrometer (JES-RE1X) equipped with an Oxford Instruments cryostat (ESR 910). The standard inductive method was employed for magnetization measurements using a pulsed magnetic field at Tohoku University, and fast pulsed magnetic fields up to 10^3 T/s were generated by a capacitor bank of 90 kJ, as described elsewhere.[2a,9] The sample was immersed in liquid ^{3}He to reach a temperature as low as 0.5 K. High-frequency ESR studies on crystalline were performed in the 94−190 GHz frequency range on a homemade spectrometer at Inst. Mater. Res., Tohoku University, where Gunn diodes were used as light sources for the high frequency in the measurements under the high magnetic fields.

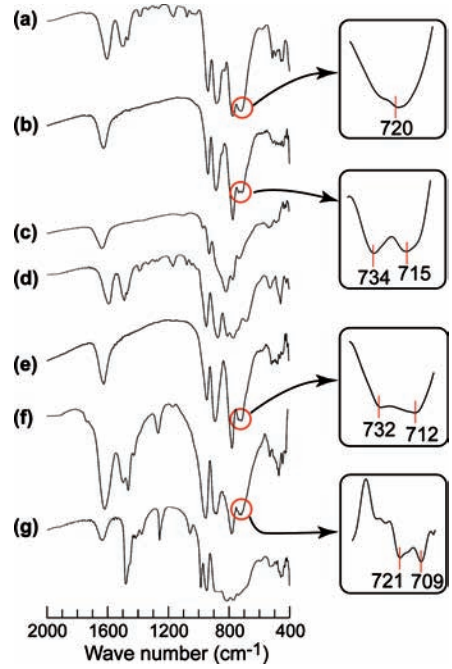

Figure 1. IR spectra of **1** (a), **2** (b), $Na_{10}[GeW_9O_{34}]\cdot 14H_2O$ (c), and solid (d) isolated by 1 h heating at 40 °C in the preparation procedure of **1**, and other solids obtained by using Cs^+ (e), $[MeNH_3]^+$ (f), and $[Me_3NH]^+$ (f), instead of $[n\text{-BuNH}_3]^+$ in the preparation procedure of **1**.

Results

Synthesis of 1. Figure 1 shows the IR spectra of **1** and **2**, together with those of $Na_{10}[GeW_9O_{34}]\cdot 14H_2O$ and other solids obtained by using other cations instead of $[n\text{-BuNH}_3]^+$. The synthesis of **1** is based on the direct reaction of B-α-$[GeW_9O_{34}]^{10-}$ (isomerized from the A-$[GeW_9O_{34}]^{10-}$ anion of $Na_{10}[GeW_9O_{34}]\cdot 14H_2O$ as a starting material)[6i] and $CuCl_2$ over 10 min at 49−50 °C in an aqueous medium containing $[n\text{-BuNH}_3]Cl$. The isolated yield for **1** is ∼18%. The formation of the B-α-$[GeW_9O_{34}]^{10-}$-sandwiched Cu_4 tetragon with a novel α-Keggin linkage was strongly favored in a shortly warmed aqueous medium, since 1 h heating of the mixture at 40 °C in aqueous media provided an unidentified pale green precipitate, the IR spectrum (Figure 1d) of which differed from the one of α-Keggin-linkage **1** (Figure 1a) or β-Keggin-linkage **2** (Figure 1b). As shown in Figure 1a and b, a broad band centered at 720 cm^{-1} due to the W−O

(8) O'Conner, C. J. *Prog. Inorg. Chem.* **1982**, *29*, 203.
(9) Nojiri, H.; Choi, K.-Y.; Kitamura, N. *J. Magn. Magn. Mater.* **2007**, *310*, 1468.

stretching vibration for the α-Keggin-linkage **1** is split into two bands centered at 715 and 734 cm^{-1} for the β-Keggin-linkage **2**. In the 1000−1500 cm^{-1} range, many absorption bands, characteristic of [*n*-BuNH$_3$]$^+$, are observed. An employment of Cs$^+$ instead of [*n*-BuNH$_3$]$^+$ in the preparation procedure gave needlelike fine crystals to exhibit the IR spectrum representative of the β-Keggin-linkage anion (Figure 1e). Similarly, use of [MeNH$_3$]$^+$ provided solids to show the IR spectrum of the two bands centered at 709 and 721 cm^{-1} representative of the β-Keggin-linkage anion (Figure 1f), while [Me$_3$NH]$^+$ provided solids of α-Keggin [GeW$_{12}$O$_{40}$]$^{4-}$ (Figure 1g;[7] also, the X-ray crystal-structure analysis of crystals obtained for a [Me$_3$NH]$^+$ salt revealed the anion of α-Keggin [GeW$_{12}$O$_{40}$]$^{4-}$). The above results suggest a significance of about a 5 Å monoalkylammonium cation in the isolation of the α-Keggin-linkage anion.

An attempt to isolate single crystals for the α-Keggin-linkage anion comprising other transition-metal tetragons failed, and the only crystals obtained were for the [*n*-BuNH$_3$]$^+$ salt of the β-Keggin-linkage anion incorporating the Mn$_4^{8+}$ tetragon, [Mn$_4$(H$_2$O)$_2$(GeW$_9$O$_{34}$)$_2$]$^{12-}$.

Description of the Structure of 1. The crystal structure of [*n*-BuNH$_3$]$_{12}$[Cu$_4$(GeW$_9$O$_{34}$)$_2$]·14H$_2$O (**1**) and the molecular structure of its anion (**1a**) are shown in Figure 2; a full listing of bond distances and angles, obtained at 300 K, are available as Tables S1 and S2 (at 10 K, Tables S3 and S4; Supporting Information). A central core of [Cu$_4$(μ_4-O)$_2$(μ_3-O)$_4$(μ_2-O)$_8$]$^{10-}$ in **1** can be described as a novel rhomblike Cu$_4$ tetragon consisting of two edge-shared CuO$_6$ octahedra at internal Cu sites (Cu$_{int}$) at a short diagonal Cu$_{int}$···Cu$_{int}$ distance of 3.111(4) Å and two CuO$_5$ square pyramids at external Cu sites (Cu$_{ext}$) at a long diagonal Cu$_{ext}$···Cu$_{ext}$ distance of 5.355(5) Å. Each square-pyramidal Cu$_{ext}$O$_5$ site is connected with two Cu$_{int}$O$_6$ octahedra by edge-sharing to form a Cu$_3$O$_{12}$ triad, which is linked with a B-α-[GeW$_9$O$_{34}$]$^{10-}$ ligand to yield the α-Keggin linkage as the α-Keggin-linkage anion. The [Cu$_4$(μ_4-O)$_2$(μ_3-O)$_4$(μ_2-O)$_8$]$^{10-}$ core differs from the [Cu$_4$(μ_4-O)$_2$(μ_3-O)$_4$(μ_2-O)$_8$(H$_2$O)$_2$]$^{10-}$ core in the β-Keggin-linkage anion for **2** where the aqua molecule is bound terminally at the Cu$_{ext}$ site to yield the Cu$_4$ tetragon consisting of four Jahn−Teller (JT)-distorted CuO$_6$ octahedra. The tungsten−oxo bond distances and angles of the structure for **1** are within the usual ranges, as shown for **2a**.[6j] If each Cu$_{ext}$O$_5$ square pyramid apically coordinates an aqua ligand in the same structural motif as in **2a**, the hypothetically coordinated water-oxygen (O$_w$) atom will be positioned at a separation of 2.2−2.3 Å from the μ_2-O(24) atom which bridges W(6) and W(7) atoms in the neighboring belt layer, as indicated in Figure 2b. Such a short O$_w$···O(μ_2) distance would cause the B-α-[GeW$_9$O$_{34}$]$^{9-}$ ligands to be rotated by 60° toward the β-Keggin linkage to yield long distances (3.00(1), 3.38(1), and 3.37(1) Å) from the nearest three oxygen atoms (two terminal and one bridging O atoms) in **2a** (Figure 2b). Since the apical coordination of the aqua ligand at the Cu$_{ext}$ site leads to a prevalence of the β-Keggin linkage,[6j] it is thus reasonable to consider that the α-Keggin linkage of the rhomblike Cu$_4$ tetragon with the B-α-[GeW$_9$O$_{34}$]$^{9-}$ ligands is determined by small energy differences between the two isomers, which would be controlled by the linkage kinetics involving both the size of cation and the temperature.

The separation of the two B-α-[GeW$_9$O$_{34}$]$^{10-}$ ligands is different for **1a** and **2a**, as indicated by the Ge···Ge distance of 5.760(5) Å for **1** and 5.732(2) Å for **2**. The molecular structure of the rhomblike Cu$_4^{8+}$ tetragon for **1a** at 300 and 10 K was compared in detail with the one (ref 6j) for **2a**, which was measured at 173 K by Kortz's group. Table 1 lists the results for the selected values of the atomic distances (in angstroms) and angles (degrees) at 300 and 10 K for the Cu$_4$ tetragon in **1**, together with the values (ref 6i) for **2** at 173 K. The schematic comparison of the central Cu$_4^{8+}$ tetragon between **1** (at 300 K) and **2** (at 173 K) is shown in Figure 3, where selected values of atomic separations (Figure 3a and b) and angles (Figure 3c) are indicated by the connectivity diagrams for the Cu$_4$O$_{14}$ and Cu$_4$O$_{16}$ fragments of **1** and **2**, respectively. The copper oxidation states are supported by the shorter average bond distances (Cu$_{int}$−O(μ_2-, μ_4-) and Cu$_{ext}$−O(μ_2-, μ_3-)) at 1.91−2.00 Å for the Cu$_{int}$ and Cu$_{ext}$ sites, and the JT-elongation axes laying on Cu$_{int}$−O(μ_3-) at 2.37−2.47 Å are nearly parallel to the Cu$_{ext}$−O(μ_4-) bonds at 2.27−2.36 Å. It is interesting that there is no significant difference in the JT-distorted CuO$_6$ octahedra (with respect to bond distances and angles) between **1** and **2**. The Cu$_{ext}$−O(μ_4-) bond length (in 2.27−2.29 Å) for **1** is significantly shorter than the corresponding bond length at the JT-distorted Cu$_{ext}$ sites for **2** (2.364(7) Å), as implied by the fact that the Ge···Ge distance (5.75−5.76 Å) for **1** is slightly longer than for **2** (5.732(2) Å). Consequently, the Cu$_{ext}$···Cu$_{ext}$ distance of 5.34−5.35 Å for **1** becomes shorter than for **2** (5.560(3) Å) containing the two JT-distorted Cu$_{ext}$O$_6$ octahedra, and the Cu$_4$ tetragon of **1** consists of two equilateral Cu$_{int}$Cu$_{int}$Cu$_{ext}$ triangles of 3.08−3.11 Å with 60° angles, in contrast to the two isosceles ones of 3.07 and 3.17 Å with with 61, 61, and 58° angles for **2**. The above structural difference of the rhomblike Cu$_4^{8+}$ tetragon between **1** and **2** gives a clue to demonstrating the magnetization behavior of the two isomers, as discussed below. As shown in Table 1, the fact that the shortest intermolecular Cu$_{ext}$···Cu$_{ext}$′ distance (8.804(1) Å) at 10 K for **1** is shorter than that at 300 K is attributed to the partial removal of the crystal water molecules from the lattice before and during the measurement, resulting in a smaller volume of the unit cell for the species formulated as [*n*-BuNH$_3$]$_{12}$[Cu$_4$(GeW$_9$O$_{34}$)$_2$]·9H$_2$O.

Magnetic Susceptibility Studies. Variable-temperature magnetic susceptibility measurements were performed on polycrystalline samples of **1** and **2** in an applied field of 0.1 T. The data are shown as $\chi_M T$ versus T plots in Figure 4. The value of $\chi_M T$ for **1** decreases from 1.35 cm^3 mol^{-1} K at 300 K to a minimum of 0.89 cm^3 mol^{-1} K at 60 K and then slightly increases to 0.91 cm^3 mol^{-1} K at 2 K. Complex **2** showed a decrease in $\chi_M T$ from 1.62 cm^3 mol^{-1} K at 300 K to a plateau around 0.95 cm^3 mol^{-1} K in the range 40−15 K, followed by a decrease to 0.90 cm^3 mol^{-1} K at 2 K. The approximate $\chi_M T$ plateau values in the low-temperature range for **1** and **2** are close to spin-only ($g = 2$) values expected

for either two separated Cu^{2+} atoms (0.75 cm^3 mol^{-1} K) or an $S = 1$ triplet state (1.00 cm^3 mol^{-1} K). The $\chi_M T$ values at 300 K are close to the sum (1.50 cm^3 mol^{-1} K corresponding to 3.46 μ_B) of spin-only contributions for four Cu^{2+} atoms.

To evaluate the Cu_4^{8+} tetragon exchange interactions within the molecule, the $\chi_M T$ versus T data for **1** and **2** were fit to the appropriate theoretical expression. The complete spin Hamiltonian (H) for the exchange interaction in the Cu_4^{8+} tetragon may be written as eq 1:

$$H = H_{iso} + H_Z + H_{asym} \quad (1)$$

where the first term is for isotropic exchange coupling, the second term is the Zeeman effect, and the third term is the asymmetric exchange coupling. The virtual C_{2h} symmetry in the solid state of these compounds requires three exchange parameters (J, J', and J''), which represent the isotropic interactions along the sides, short diagonal, and long diagonal of the rhomb. The isotropic Heisenberg spin Hamiltonian (H_{iso}) is given in eq 2, where J, $J'(= aJ)$, and $J''(= bJ)$ refer

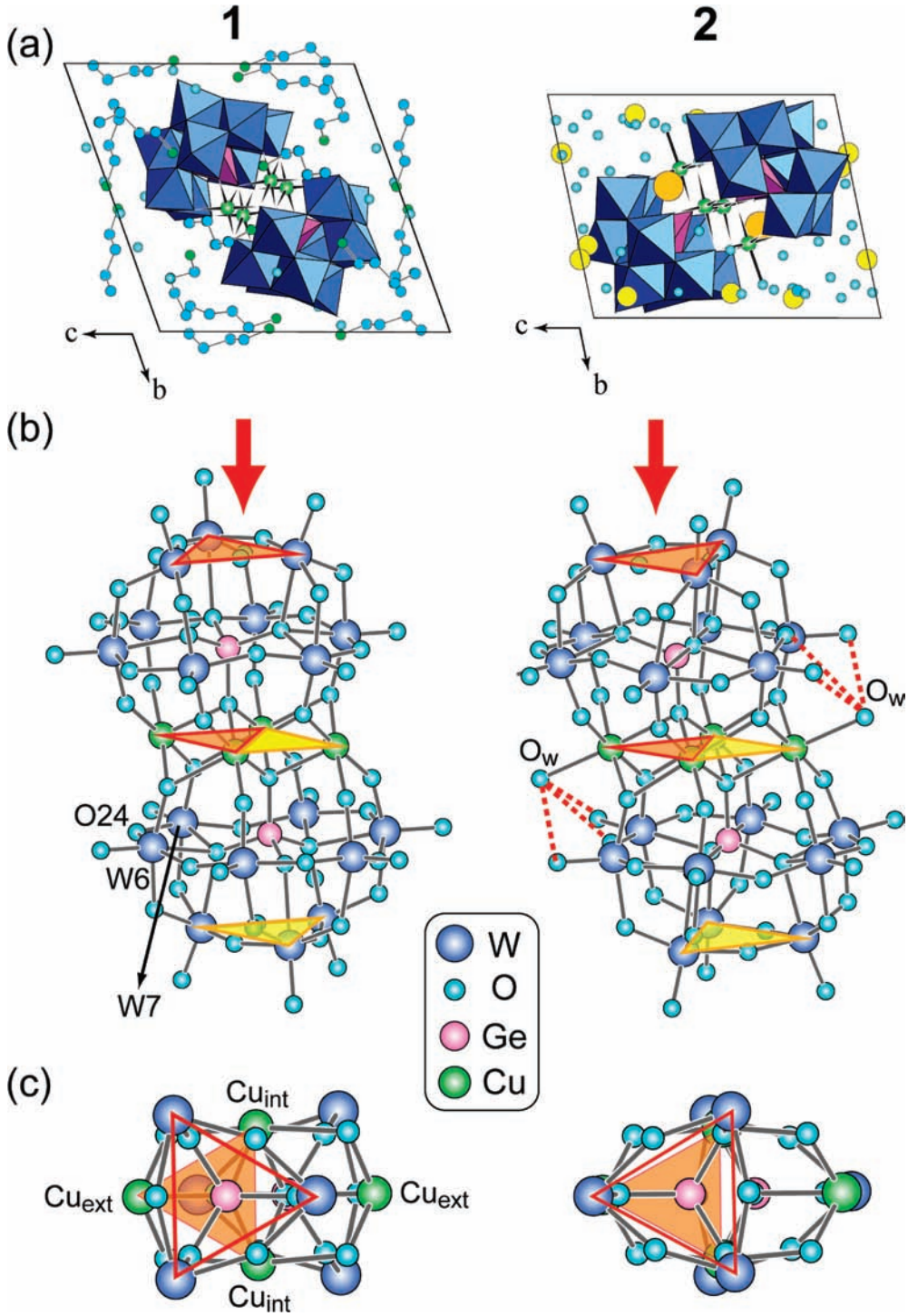

Figure 2. Crystal structures (a) and molecular structures of the anion (b) and Cu_4^{8+} tetragon (c) for **1** and **2**.

Table 1. Interatomic Distances (Å) and Angles (deg) for Cu_4^{8+} Tetragon in **1** and **2** at Selected Temperatures

	1		**2**[6j]
	300 K	10 K	173 K
Cu_{int}−O(Ge)μ_4−[a]	2.00(1), 1.99(1)	1.981(4), 2.002(4)	1.973−1.986 (8)
Cu_{int}−O(W)μ_2−[b]	1.91(1), 1.94(1)	1.914(5), 1.936(5)	1.931(8)
Cu_{int}−O(W, Cu)μ_3−[c]	2.40(1), 2.47(1)	2.374(4), 2.443(5)	2.406−2.427(8)
Cu_{ext}−O(Ge)μ_4−	2.29(1)	2.271(4)	2.364(8)
Cu_{ext}−O(W)μ_2−	1.96(1), 1.96(1)	1.943(5), 1.948(5)	1.969−1.974(8)
Cu_{ext}−O(W, Cu)μ_3−	1.96(1), 1.97(1)	1.965(5), 1.978(5)	1.966−1.988(8)
Cu_{ext}−OH_2[d]			2.346(9)
Cu_{int}···Cu_{int}	3.111(4)	3.100(1)	3.069(3)
Cu_{int}···Cu_{ext}	3.091(3), 3.102(4)	3.084(1), 3.095(1)	3.174(2), 3.176(2)
Cu_{ext}···Cu_{ext}	5.355(5)	5.344(2)	5.560(3)
Cu_{ext}−O(Ge)−Cu_{int}	92.5(5), 92.3(6)	92.2(2), 93.2(2)	95.3, 93.7(3)
Cu_{int}−O(Ge)−Cu_{int}	102.6(7)	102.2(2)	101.7(3)
Cu_{ext}−O−Cu_{int}	87.8(5), 89.9(6)	88.5(2), 89.8(2)	91.9, 92.1(3)
Cu_{ext}···Cu_{int}···Cu_{int}	59.66(9), 60.03(8)	59.71(3), 60.06(3)	61.07(5), 61.13(5)
Cu_{int}···Cu_{ext}···Cu_{int}	60.31(8)	60.23(3)	57.80(5)
Cu_{ext}···Cu_{ext}···O(Ge)μ_4−	27.7(4)	27.8(1)	26.6(2)
Ge···Ge	5.760(5)	5.748(2)	5.732(2)
Cu_{ext}···Cu_{ex}′[e]	9.264(7)	8.804(1)	8.088(3)

[a] O(Ge)μ_4− means μ_4-O atom which is coordinated by three Cu(= 2Cu_{int} + Cu_{ext}) and Ge atoms. [b] O(W)μ_2− means μ_2-O atom which is coordinated by Cu and W atoms. [c] O(W, Cu)μ_3− means μ_3-O atom which is coordinated by two Cu(= Cu_{int} + Cu_{ext}) and W atoms. [d] OH_2 means aqua ligand O atom. [e] the shortest intermolecular Cu···Cu distance.

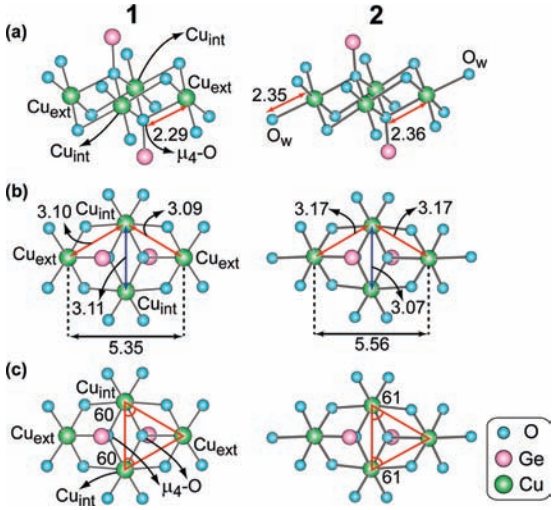

Figure 3. Connectivity diagrams for central Cu_4O_{14} and Cu_4O_{16} fragments of **1** (at 300 K) and **2** (at 173 K), respectively. Selected values of atomic separations (in Å) and angles (in deg) for the Cu_4^{8+} tetragons are indicated in parts a and b and part c, respectively. The corresponding values at 10 K for **1** are shown in Table 1.

to the exchange interactions along the sides, the short diagonal, and the long diagonal of the rhombus, respectively. The numbering scheme of the four Cu^{2+} ions for the exchange interaction in the Cu_4^{8+} tetragon is shown in the inset of Figure 4. When we take $\hat{S}_i$ to be the spin angular momentum operator for *i*th Cu^{2+} ion (in units of $h/2\pi$) with the vector sum $S_{ij} = S_i + S_j$, the Kambe vector coupling method is applicable.[10]

$$H_{iso} = -2J(\hat{S}_1\hat{S}_2 + \hat{S}_2\hat{S}_3 + \hat{S}_3\hat{S}_4 + \hat{S}_4\hat{S}_1) - 2J'\,\hat{S}_1\hat{S}_3 - 2J''\,\hat{S}_2\hat{S}_4$$
$$= -2J(\hat{S}_1\hat{S}_2 + \hat{S}_2\hat{S}_3 + \hat{S}_3\hat{S}_4 + \hat{S}_4\hat{S}_1 + a\hat{S}_1\hat{S}_3 + b\hat{S}_2\hat{S}_4) \quad (2)$$

Using the substitutions $\hat{S}_A = \hat{S}_1 + \hat{S}_3$, $\hat{S}_B = \hat{S}_2 + \hat{S}_4$, and $\hat{S}_T = \hat{S}_A + \hat{S}_B$, where S_T is the spin of the complete molecule,

(10) Kambe, K. *J. Phys. Soc. Jpn.* **1950**, *5*, 48.

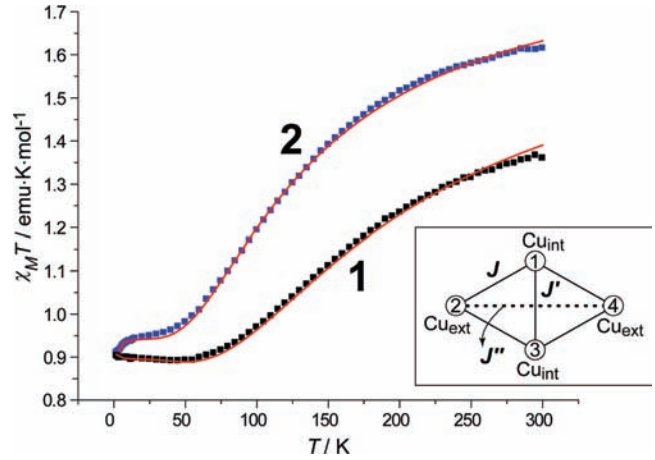

Figure 4. $\chi_M T$ vs T plots for polycrystalline samples of **1** and **2** under a 0.1 T field. The numbering scheme for the spin Hamiltonian for three exchange interactions (J−J'') of a four-spin $S = 1/2$ rhombus system is shown in the inset.

Table 2. Best-Fitting Magnetic Interaction Parameters Obtained from Simulation of $\chi_M T$ versus T Curve for **1** and **2**

	1	**2**	**2** (ref 6j)
J in cm^{-1} (in K)	–24.1 (–34.6)	–9.72 (–14.0)	–11
J' in cm^{-1} (in K)	–99.1 (–142.6)	–71.9 (–103.4)	–82
J'' in cm^{-1} (in K)	+0.04 (+0.05)	–0.11 (–0.16)	
g	2.18	2.24	2.24
agreement factor ($R_{\chi T}$)	4.78 × 10^{-5}	2.56 × 10^{-5}	

allows the eigenvalues $E(S_T, S_A, S_B)$ of eq 2 to be given by eq 3.

$$E(S_T, S_A, S_B) = -J[S_T(S_T+1) - (1-a)S_A(S_A+1) - (1-b)S_B(S_B+1) - 2(a+b)S_i(S_i+1)] \quad (3)$$

For **1** and **2**, $S_i = 1/2$; $S_A = 0$ and 1; $S_B = 0$ and 1; and $S_T = 0$, 1, and 2, and the overall multiplicity of the system is made up of individual spin states of two singlets, three triplets, and one quintet.

A theoretical $\chi_M T$ versus T expression was derived using the S_T, S_A, and S_B values; their energies $E(S_T, S_A, S_B)$; and the Van Vleck equation,[11] and this expression was used to fit the experimental data. When the highest-lying state was taken as the energy origin, the magnetic susceptibility data of **1** were analyzed using eq 4.

$$\chi_M T = (2N_A\mu_B^2 g^2/k)\{5 + \exp(2x) + \exp(x+y) + \exp(x+z)\}/\{5 + 3\exp(2x) + 3\exp(x+y) + 3\exp(x+z) + \exp(3x) + \exp(x+y+z)\} \quad (4)$$

Here, N_A is Avogadro's number, g is the g value, μ_B is the Bohr magneton, k is the Boltzmann constant, T is the temperature in Kelvin, $x = 2J/kT$, $y = 2J'/kT$, and $z = 2J''/kT$. The fit parameters are J, J', J'', and g. The best-fitting parameters obtained from a simulation of the above $\chi_M T$ versus T curve are collected in Table 2, where J, J', and J'' in are measured in centimeters^{-1} and K units and g values are represented together with the agreement factor of $R_{\chi T} = [\sum\{(\chi_M T)_{calcd} - (\chi_M T)_{obsd}\}^2/\sum\{(\chi_M T)_{obsd}\}^2]$ for **1** and **2**. Table 2 also lists the values obtained by Kortz's group, who

(11) Boča, R. Theoretical foundations of molecular magnetism. *Current Methods in Inorganic Chemistry*; Elsevier Science: Amsterdam, 1999; Vol. *1*.

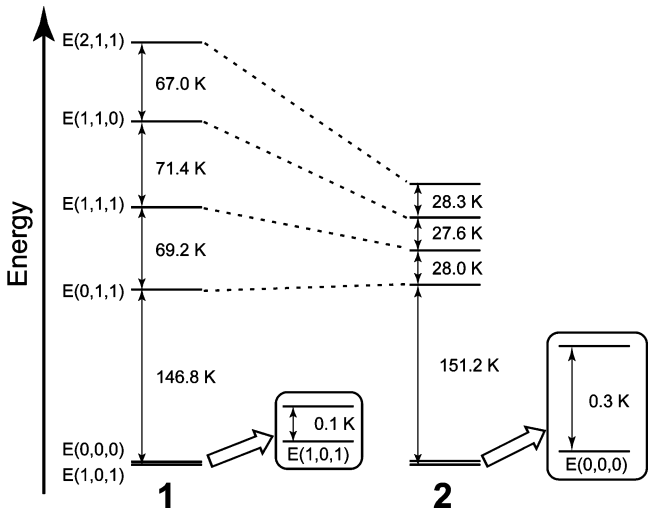

Figure 5. Energy level diagram for **1** and **2**. Labels indicate $E(S_T, S_A, S_B)$ for each level: when $E(0, 0, 0) = 0$, $E(1, 0, 1) = -2J''$, $E(0, 1, 1) = 4J - 2J' - 2J''$, $E(1, 1, 1) = 2J - 2J' - 2J''$, $E(1, 1, 0) = -2J'$, and $E(2, 1, 1) = -2J - 2J' - 2J''$.

analyzed the $\chi_M T$ versus T curve for **2** using a two-exchange parameter model comprising the Weiss constant parameter instead of J'',[6j] indicating a similarity with their results. Good fits are obtained for **1** and **2**, and these are shown by red solid lines in Figure 4. The values of the J'/J ratio for **1** and **2** are 4.1 and 7.4, respectively. Figure 5 shows the energy level diagram for **1** and **2**. As shown in Figure 4, $\chi_M T$ values for **1** are always lower than for **2**, especially at high temperatures of 100−300 K. This feature may arise from the difference in the thermal population to the highest excited state of $S = 2$ of (2,1,1), which is positioned at 354 and 235 K above the ground state of $S = 1$ at (1,0,1) or $S = 0$ at (0,0,0) for **1** and **2**, respectively. As previously pointed out for the four JT-distorted CuO_6 octahedral Cu_4^{8+} tetragons,[6c,j] it is important to note that the ground state is the two spin-doublet ($S = 1/2$) state as a result of the thermodynamically almost equal population of both (1,0,1) and (0,0,0) states, as indicated by $E(1, 0, 1) \approx E(0, 0, 0)$. Two $S = 1/2$ spins (at Cu_{ext} sites) in the ground state providing the $\chi_M T$ plateau in the low-temperature range magnetically interact to yield two states of $S = 1$ (1,0,1) and $S = 0$ (0,0,0) with a very small energy separation of $2|J''|$ (Figure 5). Thus, very weak ferromagnetic and antiferromagnetic exchange interactions ($J'' = +0.05$ and -0.16 K) are visualized at the lowest temperatures below 10 K for **1** and **2**, respectively (Figure 4). The magnetization in Bohr magnetons per mole unit at 1.8 K for **1** and **2** showed an increase with increasing dc field (B in Tesla, T) and reached a plateau of 2 μ_B, as shown in Figure 6. The magnetization behavior observed under the dc field at 1.8 K is in good agreement with the magnetization of the two spin-doublet ($S = 1/2$) state.

There is a significant difference in J between **1** and **2** (Table 2): the $|J|$ value for **1** is about twice as large as that for **2**, in contrast to the $|J'|$ value, which is similar to the value for **2**. A strong antiferromagnetic exchange interaction (with a large $|J'|$) between the short diagonal Cu_{int} sites (at $Cu_{int}\cdots Cu_{int}$ distances of 3.07−3.11 Å for the edge-shared CuO_6 octahedra) is likely to be an origin of the two

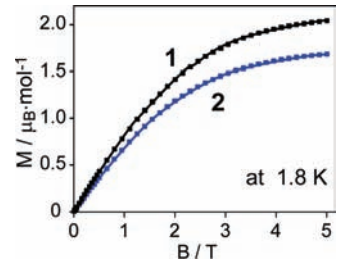

Figure 6. DC-field dependence of the magnetization in Bohr magnetons (μ_B) per mole units at 1.8 K for **1** and **2**.

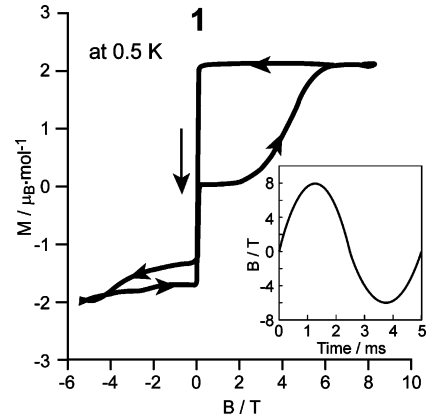

Figure 7. The magnetization curve vs pulsed magnetic field at 0.5 K for the polycrystalline of **1**. The saturated magnetization is scaled to $g\mu_B S$. The inset shows the pulsed magnetic field (**B**) versus time.

magnetically almost independent spin-doublets at long $Cu_{ext}\cdots Cu_{ex}$ distances of 5.35−5.56 Å.

Magnetic Hysteresis under Pulse Field. The magnetization behavior of **1** in nonequilibrium at the lowest temperature was investigated for the polycrystalline sample by using a pulsed magnetic field. The magnetization curve measured at 0.5 K is shown in Figure 7. The inset in Figure 7 shows the waveform of the magnetic field (B) as a full cycle sinusoid, which indicates that the field sweep rate up to 10^3 T/s is not constant in the pulsed magnetic field, and that the amplitude of B is lower on the negative side due to the dampening of the current arising from the Joule's heating in the magnet.[9] A big hysteresis in the first half-cycle, a sharp reversal at $B = 0$, and a minor hysteresis on the negative field side are found. Upon sweeping the pulsed field upwardly, the magnetization for **1** at first approaches saturation around 2 μ_B in higher fields of $B > 5$ T. Together with the ferromagnetic behavior at the lowest temperature (Figure 4), this indicates the $S = 1$ (1,0,1) ground state. The magnetization curve is much different from that expected in a dc steady field where the magnetization curve should follow the Brillouin function (Figure 6). The large deviation of the experimental curve from the Brillouin function demonstrates the nonequilibrium of the magnetization under the pulsed field. The competition between the thermal relaxation and the fast change of magnetic field is the origin of the hysteresis. The sharp reversal magnetization around $B = 0$ let us determine the negative sign of the zero-field splitting parameter (D) for the $S = 1$ (1,0,1) ground state of **1**, by assuming that the energy level for the $S = 1$ state can be expressed by a simple Zeeman crossing at $B = 0$. At the

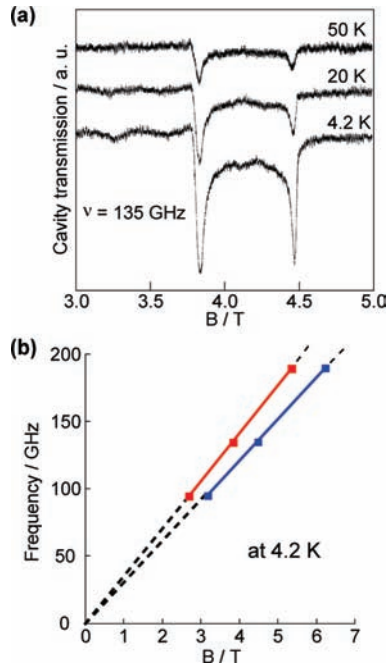

Figure 8. The 135 GHz ESR spectra of the polycrystalline sample of **1** at 4.2, 20, and 50 K (a) and plots of the experimental field positions of the resonances as a function of the frequency at 4.2 K (b).

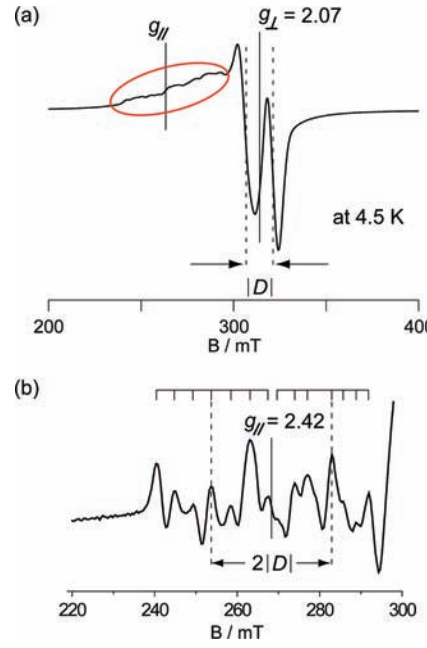

Figure 9. X-band ESR spectrum of the polycrystalline sample of **1** at 4.5 K (a) and a second derivative plot (b) of the $g_{||}$ lines, indicated by the red circle.

initial state before the pulse, the populations of the spins for the $S = 1$ (1,0,1) ground state (with $D < 0$, as discussed below) are equal between two levels of quantum numbers of projection of the spin angular momentum, $M = +1$ and $M = -1$. When the magnetic field is swept from zero upwardly, the magnetization should increase. The equilibrium value of the population is given by the partition function with two parameters: temperature and magnetic field intensity. If the sweep time is much longer than the relaxation time between the two levels, presumably through the $M = 0$ level, the magnetization should take the equilibrium value given by the Brillouin function. When the sweep rate is very fast, the equilibrium of the population at 0.5 K cannot be achieved. In the fast sweeping limit, no relaxation occurs, and the initial equal population must be kept. This would result in zero magnetization because the magnetizations of spins in the two levels cancel each other. As shown in Figure 7, the magnetization below 3 T indicates that the relaxation time is much longer than the time period (about 0.5 ms) of the field sweep. When the sweep rate becomes zero at the maximum of $B = 8$ T, the relaxation comes into effect around this point. In the down sweep after the magnetization saturation of 2 μ_B, the magnetization is nearly constant, and then it shows a very rapid reversal at $B = 0$. The field sweep rate becomes faster again toward $B = 0$ for the oscillating behavior. Since the thermal relaxation is quenched in this region, the rapid magnetization reversal at $B = 0$ can be attributed to the quantum tunneling and is not expressed by the Brillouin curve, which can be applied only for the equilibrium magnetization process. If there is no tunneling, the magnetization should be positive, even on the negative field side.

ESR Spectroscopy. Figures 8 and 9 show results of high-frequency and X-band ESR measurements on a polycrystalline sample of **1**. The 135 GHz ESR spectra at 4.2, 20, and 50 K reveal two resonances at $g = 2.52$ and 2.16 (Figure 8a), and the extrapolation of the field position of two resonances as a function of frequency (from 190 to 94 GHz) to zero field at 4.2 K leads to coincidence of the two positions around $B = 0$ (Figure 8b). Since the unit cell (with $Z = 1$ and space group of $P\bar{1}$) of **1** contains one molecule, and therefore one easy magnetization direction for the crystallites is expected, it is clear that the two signals on the high-frequency ESR spectra are attributed to g-anisotropy and that the $|D|$ expected for the $S = 1$ state is small enough to be hidden within the experimental line width. Some ESR parameters of the nearly axially symmetric resonances of **1** appear on the 4.5-K X-band ESR spectrum (Figure 9a), which shows the $S = 1$ state with small values of $|D|$ and hyperfine features (A): The X-band ESR spectrum consists of the broadly overlapping low-field parallel (||) lines (comprising ^{63,65}Cu-hyperfine features) and the two high-field perpendicular ($\perp$) lines (separated by 14.9 mT due to $|D|$). In the first approximation, we assume that the system is axially systematic and write the appropriate $S = 1$ Hamiltonian as follows using eq 5:

$$H_Z + H_{asym} + H_{hf} = \beta[g_{||}B_zS_z + g_{\perp}(B_xS_x + B_yS_y)] + D[S_z^2 - S(S+1)/3] + A_{||}S_zI_z + A_{\perp}(S_xI_x + S_yI_y) \quad (5)$$

where the H_{hf} term is for the ^{63,65}Cu-hyperfine interaction, and other symbols have their usual meaning. Of interest is the progression of approximately 14 lines, which follows the low-field parallel lines, $|A_{||}|$ (with average spacing 4.1 mT), as positioned by 14 minima resolved from the second derivative plot (Figure 9b) of ^{63,65}Cu-hyperfine structure. We can evaluate ESR parameters for **1**, as listed in Table 3, where similar parameters estimated from the 4.4 K X-band ESR signal for **2** are shown for comaparison.[6j] The average

Table 3. ESR Parameters Obtained for **1** and **2**

	1	**2** (ref 6j)
$g_{\|\|}$	2.42	2.43
$g_{\perp}$	2.07	2.06
$<g> = (2g_{\perp} + g_{\|\|})/3$	2.18	2.18
$\|D\|$ in cm^{-1} (in K)	0.0144 (0.0209)	0.012 (0.017)
$\|A_{\|\|}\|$ in cm^{-1} (in mK)	46.5×10^{-4} (6.7)	42.2×10^{-4} (6.1)

value of g, $<g> = (2g_{\perp} + g_{\|\|})/3 = 2.18$, is in good agreement with the above analysis for the $\chi_M T$ versus T plot (Table 2). Having no observation of the hyperfine perpendicular lines ($|A_{\perp}|$) is due to their small splitting hidden within the line width.

It is noted that the 135-GHz ESR spectra of **1** showing two distinct lines at $g_{\|} = 2.52$ and $g_{\perp} = 2.16$ give a stronger resonance at low fields (Figure 8a), in contrast to the ones ($g_{\|} \approx 2.43$, $g_{\perp} = 2.08$, and $<g> = 2.16$) of **2**, with a sharper and stronger line at higher fields (Figure S1, Supporting Information). The polycrystalline sample of **1** was fairly loosely packed, and we suspect that this was due to the field alignment of a significant number of the crystallites, which led to an enhancement of the easy (*z*-) axis components of the spectrum relative to the hard (*xy*-) plane response. Together with an observable enhancement of the low-field line with increasing ESR frequency (data not shown), such an alignment of a fraction of the crystallites thus resulted in stronger and sharper parallel resonances relative to perpendicular lines. In addition, the displacement of g values (2.33 as average g, for example) for the high-frequency ESR lines of **1** from those for the X-band lines suggests an occurrence of the level mixing (with other excited states) at high fields of $B > 2$ T, which makes a simple Kambe−Heisenberg model no longer adequate for evaluation of the g value.

Discussion

Both Cu_{int} and Cu_{ext} sites in the rhomblike Cu_4^{8+} tetragon of **1** are axially distorted in such a way that the long axes of the CuO_6 octahedra and CuO_5 square pyramids are parallel, and the distortion for the CuO_5 square pyramid is smaller than the JT distortion imparted by the coordination of aqua ligands at the Cu_{ext} sites in **2** (Figure 3). The decrease in distortion for **1**, which is induced by replacing the JT CuO_6 octahedron with the CuO_5 square pyramid at the Cu_{ext} site, results in a shortening (from 5.56 to 5.34−5.36 Å) of the $Cu_{ext}\cdots Cu_{ext}$ distance (Table 1). Since the magnetic exchange interactions for the rhomblike Cu_4^{8+} tetragon are strongly related to the Cu···Cu distance, the above magnetic features for **1** and **2** give us a good opportunity to discuss pathways of the magnetic exchange interactions in the Cu_4^{8+} tetragon, which have never been investigated in conjunction with the $Cu_{ext}\cdots Cu_{ext}$ distance.[6c,j] The magnetic susceptibility analysis by use of the isotropic Heisenberg model with three magnetic-exchange parameters indicates a ground state of the $S = 1$ (1,0,1) triplet for **1** and the $S = 0$ (0,0,0) singlet for **2**, with a very small zero-field splitting energy of 0.1 and 0.3 K from the nearest excited state of the singlet and the triplet, respectively (Figure 5). These two states are thermodynamically almost equally populated in the range 20−50 K at $B = 0$, resulting in the two independent $S =$

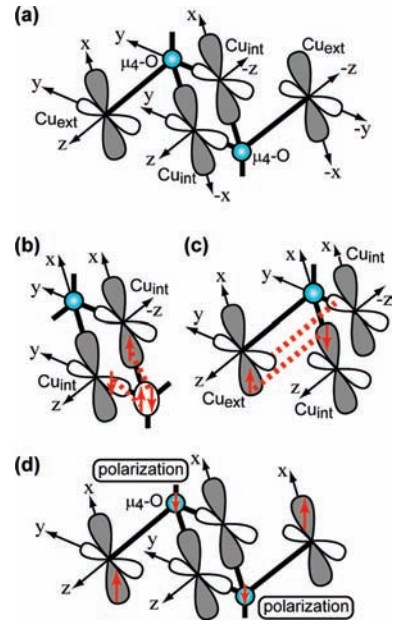

Figure 10. Orientation of the $d_{x^2-y^2}$ orbital superimposed on both Cu_{int} and Cu_{ext} sites in the Cu_4^{8+} tetragon (a) and schematic presentations (b−d) of magnetic interactions among the Cu sites.

1/2 spin doublets with random spin alignment at long diagonal Cu_{ext} sites, which are separated by the short diagonal $S = 1/2$ spins aligned strongly antiparallel ($|J'| = 103-143$ K) at the Cu_{int} sites. As shown in Table 1, this antiferromagnetic interaction J' between the Cu_{int} sites at a $Cu_{int}\cdots Cu_{int}$ distance of 3.07−3.11 Å is much stronger than between the Cu_{int} and Cu_{ext} sites ($J = -35$ K for **1** and −14 K for **2**). Figure 10 shows the schematic orientation of four $d_{x^2-y^2}$ unpaired electron orbitals at both the Cu_{int} and Cu_{ext} sites in the Cu_4^{8+} tetragon and the schematic interactions of the magnetic electrons. As shown in Figure 10a, the orientation of three $d_{x^2-y^2}$ orbitals for two $Cu_{ext}(Cu_{int})_2$ triads in the rhomblike Cu_4^{8+} tetragon for **1** and **2** is not equivalent. This excludes the possibility of the magnetic spin frustration which was previously suggested.[6j] Also, neither a broadening nor a shift of the high-frequency ESR line (Figure 8 and Figure S1, Supporting Information) at low temperatures, suggesting the absence of short-range ordering, excludes the possibility of spin frustration within the $Cu_{ext}(Cu_{int})_2$ triangle.[5b] The strong antiferromagnetic interaction between the edge-shared JT-CuO_6 octahedra at the Cu_{int} sites results from an involvement of two $d_{x^2-y^2}$ orbitals in the σ bond on the *xy* plane of the edge-shared $Cu_{int}O_6$ octahedra, as proposed previously:[6c] the two $d_{x^2-y^2}$ unpaired electron orbitals at the Cu_{int} atoms are approximately pointing toward the bridging μ_4-O atoms to form σ bonds with sp^3-like orbitals at the μ_4-O atoms,[12] allowing a large overlap integral to give the strong superexchange antiferromagnetic interaction between the Cu_{int} spins, as illustrated in Figure 10b. The J value for **1** is about twice as strong as that for **2**, which is associated with the direct interaction between the unpaired

(12) For simplification, bonding orbitals of the μ_4-O atom are assumed to be sp^3-hybrid: Ge−O(μ_4-)−Cu of 117.6(7)°, 122.0(7)°, and 122.4(6)° and Cu−O(μ_4-)−Cu bond angles of 92.5(5)°, 92.3(6)°, and 102.6(7)° for **1** (Table 2S, Supporting Information).

electron orbitals at both the Cu_{ext} and Cu_{int} sites. As shown in Table 1, a shorter $Cu_{ext}-O(\mu_4\text{-})$ distance of 2.29 Å (2.27 Å at 10 K) for **1** favors δ-like antiferromagnetic interaction between the $d_{x^2-y^2}$ orbitals at the Cu_{ext} and Cu_{int} sites (Figure 10c), compared with the case of the JT distance (2.36 Å) for **2**.

The weak ferro- and antiferromagnetic behavior at the lowest temperatures below 10 K for **1** and **2**, respectively, is interesting. The difference in the axially distorted $Cu-O(\mu_4\text{-})$ distance at the Cu_{ext} sites gives us a clue to demonstrating the magnetism of **1** and **2** at the lowest temperatures. It is likely that the long $Cu_{ext}-O(\mu_4\text{-})$ distance of 2.36 Å at the JT-distorted CuO_6 octahedron for **2**, resulting in a long separation (isolated at a $Cu_{ext}\cdots Cu_{ext}$ distance of 5.56 Å) of the two $S = 1/2$ spins in the Cu_4^{8+} tetragon, makes a weak antiferromagnetic interaction between the two spins to form the $S = 0$ (0,0,0) ground state. Assuming the point-dipole approximation in the case of the shorter $Cu_{ext}-O(\mu_4\text{-})$ distance for **1**, on the other hand, the paramagnetic electron $d_{x^2-y^2}$ orbital at the Cu_{ext} atom in the axially distorted CuO_5 square pyramid gives rise to the spin polarization on the axial μ_4-O atom through Hund's and Pauli principles. As a result, a negative spin-density at the μ_4-O atomic orbitals which form σ bonds with the $d_{x^2-y^2}$ orbitals on the *xy* plane of two $Cu_{int}O_6$ octahedra could lead to a parallel orientation of the paramagnetic electron spin on the $d_{x^2-y^2}$ orbital at the other Cu_{ext} site. Such a net unbalance (with same sign) of spins on the axial μ_4-O atoms in the axially distorted CuO_5 square pyramids could rationalize the ferromagnetic interaction of the two $S = 1/2$ states between the Cu_{ext} sites. Figure 10d shows a scheme proposed for the ferromagnetic interaction between the two $S = 1/2$ spins at the Cu_{ext} sites for **1**.

Next, we try to determine the sign of D for the $S = 1$ (1,0,1) states of **1** and **2**. The sharp reversal magnetization of nearly $|2|\mu_B$ around $B = 0$ on the magnetization curve at 0.5 K under the pulsed field (Figure 7) reveals $D < 0$ for the $S = 1$ (1,0,1) ground state of **1**, because the zero-magnetization through the level crossing (due to the spin-allowed transition of $\Delta M = \pm 1$) between $M = \pm 1$ and $M = 0$ levels around $B = 0$, which would be the case for $D > 0$, was not observed. A similar feature of the magnetization under the pulse field was obtained for **2**, indicating $D < 0$, as shown in Figure S2 (Supporting Information) where the observable depression of the magnetization rationalizes the $S = 1$ (1,0,1) state as the excited state for **2**, which is positioned at around 0.3 K ($= 2|J''|$) above the $S = 0$ (0,0,0) ground state at $B = 0$ (Figure 5). Figure 11 shows schematic views of the energy levels (at a magnetic field parallel to the long axis of the $Cu_{ext}O_5$ square pyramid) of the $S = 1$ (1,0,1) state around $B = 0$, when $D < 0$ (a) and $D > 0$ (b). For $D < 0$, the energy gap between the $M = -1$ and $M = +1$ levels at $B = 0$ demonstrates the quantum tunneling around $B = 0$ (Figure 11a), while for $D > 0$ the zero magnetization of the ground state through the level crossing with the $M = 0$ level around $B = 0$ should be expected (Figure 11b). The analysis of the tunneling gap at $B = 0$ for $D < 0$ remains for further investigation: the coupling between the electron spin and the nuclear spin to yield the composite

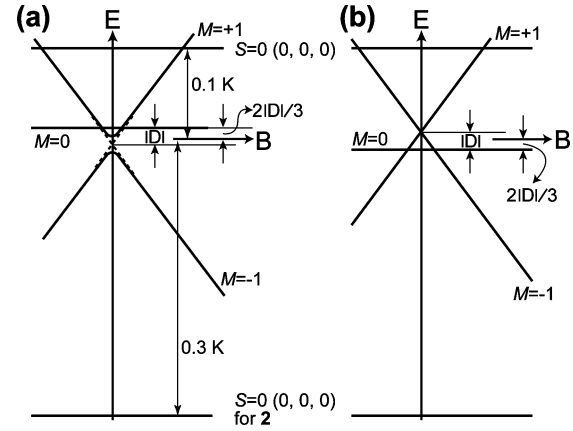

Figure 11. Schematic views of the energy levels of $M = \pm 1$ and $M = 0$ for the $S = 1$ (1,0,1) state around $B = 0$ at a magnetic field parallel to the long axis of the $Cu_{ext}O_5$ square pyramid, when $D < 0$ (a) and $D > 0$ (b). A zero field gap between $M = -1$ and $M = +1$ levels is also indicated for demonstrating the quantum tunneling at $B = 0$ (a). The energy levels for the $S = 0$ (0,0,0) state for **1** (black) and **2** (blue) are indicated for comparison (Figure 5).

spin system in the Cu^{2+} ion (as supported by the observation of the hyperfine features in Figure 9b) is a unique candidate for the origin of the zero-field quantum tunneling found in the $S = 1$ (1,0,1) state.[9] $D < 0$ for **2** was previously suggested by the 2 K powder W-band (94.3 GHz) ESR spectrum, showing a singletlike asymmetric (not doublet lines) signal of a more intensive line at low fields as the parallel transition.[6j]

The point-dipole approximation, which above was used to elucidate the ferromagnetic interaction between the two $S = 1/2$ spins at the Cu_{ext} sites (Figure 10d), let us discuss an origin of D of the Cu_4^{8+} tetragon. Attributing D (in cm^{-1} units) to the magnetic dipolar interaction between the Cu_{ext} sites, we can estimate it from eq 6[13]

$$|D| = (0.325g^2/r^3)(|1 - 3\cos^2\theta|) \qquad (6)$$

where r (in Å unit) is the interelectronic distance and θ is the angle between the $Cu_{ext}\cdots Cu_{ext}$ direction and the magnetic field. From the crystal structure of **1**, $r = 5.344$ Å (at 10 K) and the $Cu_{ext}-Cu_{ext}-O(\mu_4\text{-})$ angle is 27.8° (Table 1). Taking $B_{\|}$ to be along the $Cu_{ext}-O(\mu_4\text{-})$ direction, that is, $\theta = 27.8°$, one calculates $|D_{calcd}| = 0.0167$ cm^{-1} (when $g = g_{\|} = 2.42$), being in better agreement with the value (0.0144 cm^{-1}) obtained by the 4.5 K polycrystalline measurement (Table 3) in comparison with the $\theta = 0$ value ($|D_{calcd}| = 0.0248$ cm^{-1}). This would seem to imply that the $g_{\|}$ direction is close to the $Cu_{ext}-O(\mu_4\text{-})$ direction rather than the $Cu_{ext}\cdots Cu_{ext}$ direction, suggesting that the assumption of axial symmetry is not strictly true (as indicated by bond distances and bond angles at 10 K in Tables S3 and S4, Supporting Information). Similarly, $|D_{calcd}| = 0.0156$ cm^{-1} on $\theta = 26.6°$ for **2**. Together with a small value (0.0004 cm^{-1} for **1**) of the calculated pseudodipolar term (originating in spin−orbit coupling),[14] it is thus apparent that the primary contribution to the D value for the $S = 1$ (1,0,1) state comes from magnetic dipole−dipole interactions between the

(13) Stevens, K. W. H. *Proc. R. Soc. London* **1952**, *A214*, 227.
(14) Bleaney, B.; Bowers, K. D. *Proc. R. Soc. London* **1952**, *A214*, 451.

electrons located on the Cu_{ext} sites in the Cu_4^{8+} rhombus, where the strong antiferromagnetic interactions for the $Cu_{ext}\cdots Cu_{int}$ and $Cu_{int}\cdots Cu_{int}$ pairs with short Cu···Cu distances (3.1 Å) lead to the ferromagnetic interaction between the two $S = 1/2$ spins at long diagonal Cu_{ext} sites (at Cu···Cu distances of 5.3 Å) with little contribution to the D value at low temperatures $T < 40$ K.

The hyperfine structures in the powder X-band ESR spectrum of **1** at 4.5 K (Figure 9b) would arise from the combined contributions from both sites of Cu_{ext} and Cu_{int} for the $S = 1$ (1,0,1) state. Under the approximation that the hyperfine tensor is axial with $|A_{\|}| = 46.5 \times 10^{-4}$ cm^{-1} and a negligibly small value of $|A_{\perp}|$ (Table 3), defining an anisotropic hyperfine parameter for d orbitals as $7(|A_{\|}|)/6$ and dividing its value, 54.3×10^{-4} cm^{-1}, by the anisotropic hyperfine parameter $P = g\beta\gamma_{Cu}\langle r^{-3}\rangle_{3d}$ for ^{63,65}Cu (1197 MHz $= 399.3 \times 10^{-4}$ cm^{-1}) gives an estimate of 0.136 for the spin population in the Cu 3d orbitals.[15] The derived isotropic component A_{iso} ($\approx 1/3|A_{\|}| = 15.5 \times 10^{-4}$ cm^{-1}) provides a Cu 4s contribution of 0.008, when the isotropic hyperfine interaction (5995 MHz $= 1999.7 \times 10^{-4}$ cm^{-1}) for unit spin density in a Cu 4s orbital is employed.[15] As we previously analyzed the ESR parameters for the polyoxomolybdates in a similar way,[16] the point-dipole approximation in analyzing $A_{\|}$ thus gives the total spin density for the Cu_{ext} atom as 0.144 (= 0.136 + 0.008), suggesting delocalization of the paramagnetic electron over the rhomb-like Cu_4^{8+} tetragon. Since the mononuclear Cu^{2+} center shows an $|A_{\|}|$ value of 176×10^{-4} cm^{-1},[17] in addition, the observed hyperfine splitting for **1** is about 26% (= 46.5/176) of the $|A_{\|}|$ value of an isolated Cu^{2+} site, and thereby the two unpaired electrons in the $S = 1$ (1,0,1) state are implied to be delocalized over all four ($\approx$1/0.26) Cu^{2+} sites.[18] A partial displacement from the equal spacing for the 14 minima positions on the second derivative of the X-band ESR for **1** (Figure 9b) may be caused by the contributions from the Cu_{int}-hyperfine lines. However, no attempt has yet been made to adjust spin density distribution in the Cu_4^{8+} tetragon for the hyperfine structures in the powder X-band ESR spectrum.[19]

Acknowledgment. This work was supported by Grants-in-Aid for Scientific Research, Nr. 17002006 from the Ministry of Education, Science, Sports, and Culture. We thank Professor H. Takeuchi at the Toyota Institute of Technology for stimulating discussions on the ESR spectra.

Supporting Information Available: Tables S1 and S2 (bond distances and bond angles at 300 K for **1**) and Tables S3 and S4 (bond distances and bond angles at 10 K for **1**), Figure S1 (135 GHz ESR spectra of **2**) and Figure S2 (magnetization curve under the pulsed field at 0.5 K for **2**), and CIF data. This material is available free of charge via the Internet at http://pubs.acs.org.

IC8013267

(15) Morton, R.; Preston, K. F. *J. Magn. Reson.* **1979**, *30*, 577.
(16) Yamase, T.; Suga, M. *J. Chem. Soc., Dalton Trans.* **1989**, 661.
(17) Abragam, A.; Bleaney, B. *Electron Paramagnetic Resonance of Transition Ions*; Clarendon Press: Oxford, U.K., 1970.
(18) Yoon, J.; Mirica, L. M.; Stack, T. D. P.; Solomon, E. *J. Am. Chem. Soc.* **2004**, *126*, 12586.
(19) Belinsky, M. *Inorg. Chem.* **2004**, *43*, 739.